Title

Structure and photophysics of indigoids for singlet fission: Cibalackrot

Permalink

https://escholarship.org/uc/item/3n45b828

Journal

The Journal of Chemical Physics, 151(18)

ISSN

0021-9606

Authors

Ryerson, Joseph L
Zaykov, Alexandr
Suarez, Luis E Aguilar
et al.

Publication Date

2019-11-14

DOI

10.1063/1.5121863

Peer reviewed

Structure and Photophysics of Indigoids for Singlet Fission: Cibalackrot

Joseph L. Ryerson,[a,b] Alexandr Zaykov,[c,d] Luis E. Aguilar Suarez,[e] Remco W. A. Havenith,[e,f] Brian R. Stepp,[a] Paul I. Dron,[a] Jiří Kaleta,[c] Akin Akdag,[a] Simon J. Teat,[g] Thomas F. Magnera,[a] John R. Miller,[h] Zdeněk Havlas,[c] Ria Broer,[e] Shirin Faraji,[e]* Josef Michl,[a,c]* and Justin C. Johnson[b]*

[a] Department of Chemistry, University of Colorado, Boulder, Colorado 80309, USA; [b] National Renewable Energy Laboratory, Golden, Colorado 80401, USA; [c] Institute of Organic Chemistry and Biochemistry, Czech Academy of Sciences, Flemingovo nám. 2, 16610 Prague 6, Czech Republic; [d] University of Chemistry and Technology Prague, Technická 5, 16628 Prague 6, Czech Republic; [e] Zernike Institute for Advanced Materials, University of Groningen, Nijenborgh 4, 9747AG Groningen, The Netherlands, [f] Stratingh Institute for Chemistry, University of Groningen, 9747 AG Groningen, The Netherlands, [g] Advanced Light Source, Lawrence Berkeley National Lab, 1 Cyclotron Rd, Berkeley, CA 94720, USA; [h] Chemistry Department, Brookhaven National Laboratory, Upton, New York 11973, USA

Corresponding Authors' Email: Shirin Faraji, s.s.faraji@rug.nl; Josef Michl, josef.michl@colorado.edu; Justin C. Johnson· Justin.Johnson@nrel.gov

Abstract

We report an investigation of structure and photophysics of thin layers of cibalackrot, a sturdy dye derived from indigo by double annulation at the central double bond. Evaporated layers contain up to three phases, two crystalline and one amorphous. Relative amounts of all three have been determined by a combination of X-ray diffraction and FT-IR reflectance spectroscopy. Initially excited singlet state rapidly produces a high yield of a transient intermediate whose spectral properties are compatible with charge-transfer nature. This intermediate more slowly converts to a significant yield of triplet, which however does not exceed 100% and may well be produced by intersystem crossing rather than singlet fission. The yields were determined by transient absorption spectroscopy and corrected for effects of partial sample alignment by a simple generally applicable procedure. Formation of excimers was also observed. In order to obtain guidance for improving molecular packing by a minor structural modification, calculations by a simplified frontier orbital method were used to find all local maxima of singlet fission rate as a function of geometry of a molecular pair. The method was tested at 48 maxima by comparison with the ab initio Frenkel-Davydov exciton model (AIFDEM).

Singlet fission[1,2] (SF) is a molecular analog of multiple exciton generation observed in

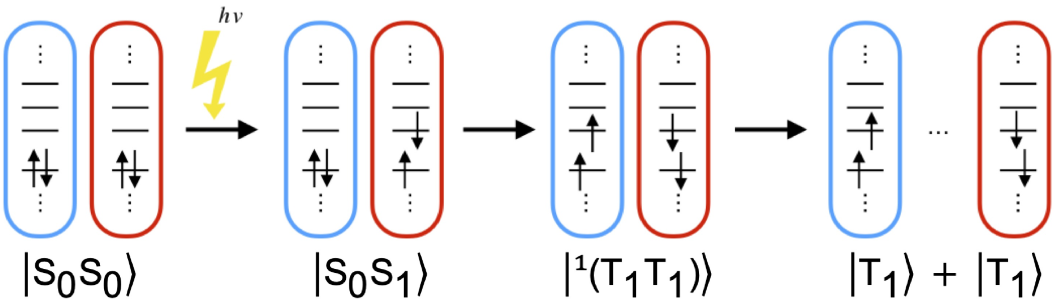

Figure 1. Schematic representation of the SF process in an organic solid. After absorption of a photon, a singlet-excited molecule (S_1) transfers some of its energy to a ground state neighbor (S_0) to form two singlet-coupled triplets ($^1T_1T_1$) in a spin-allowed process. The coupled triplets then dissociate to form free triplet excitons ($T_1 + T_1$).

semiconductor nanocrystals.[3] In the simplest description, a singlet excited molecule shares its energy with a neighboring ground state molecule to form two triplet excitations initially coupled into an overall singlet, which then separate in space and ultimately lose their spin coherence to form two independent triplet excitons[4,5,6,7,8,9,10,11,12] (Figure 1). The spin-allowed nature of SF allows it to proceed on a scale of ps or even shorter. In favorable cases, it is able to outcompete all other forms of excited singlet state decay and produce a triplet yield of 200%. This requires SF to be slightly exoergic or at most only weakly endoergic, $\Delta E(S_1) \geq 2\ \Delta E(T_1)$.

Much of the current interest in SF is due to its potential as one of the methods[13] for overcoming the Shockley-Queisser limit[14] of ~1/3 to the maximum theoretical efficiency of a single-junction solar cell. A combination of a layer absorbing high-energy photons and performing isoergic SF, ultimately converting each into two electron-hole pairs, with an ordinary layer absorbing low-energy photons and yielding a single electron-hole pair from each, should provide a theoretical efficiency close to 1/2.[15] SF exoergicity is wasteful and would reduce the cell efficiency.[16,17] Although the production of more than one electron hole-pair from a single photon by SF[18,19,20,21] has already been demonstrated, practical utilization of SF is awaiting the development of materials that not only produce triplet excitons in a yield very close to 200%, but also meet all other requirements for use in solar cells. Long-term stability under operating conditions is a particular concern, and efficient capture of the generated electrons and holes at electrodes is another.

Design of new SF materials involves three tasks: (i) identifying chromophores whose energy levels come close to meeting the requirement $\Delta E(S_1) = 2\ \Delta E(T_1)$ for the singlet and triplet excitation energies, (ii) making sure that their packing in the solid is optimal, and (iii) assuring an efficient transfer of the generated charges to electrodes. The intermolecular interactions engendered by the packing need to secure a large value for the electronic matrix element for SF while at the same time preserving the required relation between the singlet and triplet excitation energies present in an isolated molecule. In practice, the latter condition is most readily met by a packing that results in a very small excitonic level splitting.

While rules for a packing of a molecular pair that is optimal for SF have only emerged relatively recently,[22,23,24] two promising structural classes of chromophores, large aromatic hydrocarbons and biradicaloids, were identified early on. Biradicaloids are a particularly intriguing choice.[25] In a perfect biradical, the highest occupied molecular orbital (HOMO) is degenerate with the lowest unoccupied molecular orbital (LUMO) and the pair contains two electrons. The energy difference $2\Delta E(T_1)$ is then usually much too small (and often actually negative, with T_1 below S_0). In contrast, in an ordinary molecule with a large HOMO-LUMO gap, this energy difference is usually much too large relative to $\Delta E(S_1)$. Upon going from the former to the latter situation continuously by gradually introducing a covalent perturbation,[26] producing a biradicaloid in the process, one necessarily goes through a region of perturbation strengths in which the condition $\Delta E(S_1) = 2\ \Delta E(T_1)$ is satisfied. Thus, one needs to introduce just the right degree of covalent interaction between the two radical centers. The simple 3×3 model of biradicaloid electronic structure[26,27] has been used to put this argument on a semiquantitative level,[28,29,30,31] and it has been shown how simultaneous substitution of each radical center with an electron donor and acceptor (captodative substitution[32]) can be used to tune the HOMO-LUMO gap.[33]

Indigo (**1** in Figure 2) is an example of a very stable dye that has been considered for singlet fission[4] as a prime example of a captodatively stabilized biradicaloid with suitable singlet and triplet excitation energies. Unfortunately, it is disqualified as a candidate for SF by its propensity for fast photochemistry, associated both with twisting around the central double bond and proton transfer from nitrogen to oxygen.

Both of these deactivating paths are blocked in a derivative, cibalackrot (**2**, Ciba Lake Red B, 7,14-diphenyldiindolo[3,2,1-de;3',2',1'-ij][1,5]naphthyridine-6,13-dione), a sturdy industrial dye that has been known for over a century[34,35] and has been proposed for singlet fission.[5] Its solution properties appear favorable: cyclic voltammetry revealed an electronic band gap of about 2.5 eV, compared to an optical band gap of 2.0 – 2.1 eV.[36] The peak molar absorption coefficient in the visible spectrum is 21 360 $M^{-1}cm^{-1}$, the solution fluorescence quantum yield is ~0.8, and the fluorescence lifetime is 6.10 ns.[37]

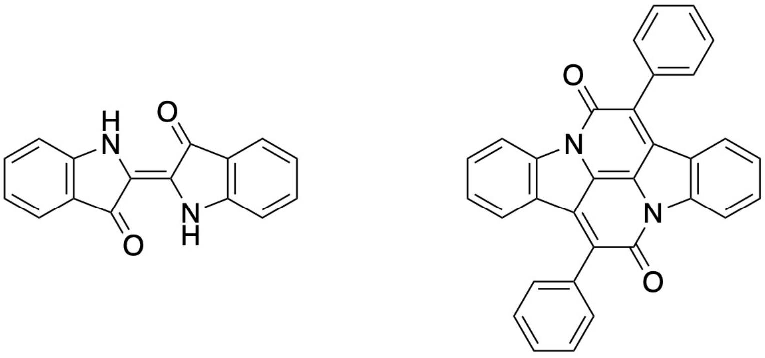

1

2

Figure 2. Structures of indigo (**1**) and cibalackrot (**2**).

Presently, we report an investigation of the photophysical properties of thin solid layers of **2**. We describe two polymorphs and an amorphous phase and show how a combination of X-ray diffraction and FTIR spectroscopy permits a quantitative determination of the fractions of the various phases in the thin layer. Ultrafast transient spectroscopy shows that singlet excited **2** does not form triplets directly but through a charge-transfer intermediate, identified by comparison with the absorption spectra of the radical ions of **2**. At the same time, emission spectroscopy provides evidence for formation of an excimer.

Quantum yields of the charge-transfer intermediate and the triplet are determined with due consideration of the partial orientation of the molecules of **2** relative to the surface of the substrate. A simple and efficient treatment of the orientation effects is described. The yields are not sufficiently high to provide conclusive evidence for SF and it is possible that the triplets are formed by rapid intersystem crossing. The excimer does not have a clear signature in the transient absorption spectra and its quantum yield has not been determined.

It appears clear that the decay of the initially excited state S_1 into the charge-transfer and excimer states competes successfully with one-step SF, and it is likely that a suitable adjustment of crystal structure might ameliorate the situation. In an effort to guide such crystal engineering we have also performed an exhaustive computational search for local maxima of the SF rate within the six-dimensional space of physically possible pair geometries. This search revealed ~1400 pair geometries, most of them far more favorable than the geometries found in the two presently known crystal forms, primarily because they avoid large excitonic splitting and the resulting endothermicity of the SF process. These calculations relied on a simplified form of the frontier orbital model limited to pairwise interactions only, and were verified by comparison with the results of ab initio Frenkel-Davydov exciton model[38] calculations at the best 48 geometries. Together, the methods provide guidance for future attempts to improve the SF performance of **2** by crystal engineering or by the use of covalent dimers.

Results

Solid structures. Sublimation of **2** yielded two polymorphs distinguishable by visual inspection. The main constituent, **2α**, consisted of very brittle long crystals that split into multiple fibrous strings when mechanically stressed. The minority crystals, **2β**, were prism-shaped, and fractured into well shaped crystals. Bulk crystals of **2** were also grown from solution and the same two polymorphs, monoclinic $P2_1/n$ (**2α**) and monoclinic $P2_1/c$ (**2β**), were found (the Supporting Information provides a detailed characterization and structural information). Closest slip-stacked molecular pairs from each crystal structure are shown in Figure 3. The phenyl substituents in **2α** are arranged in a conrotatory fashion when viewed from the center of the molecule and form an angle of 54.7° with the planar core. In **2β** they are arranged in a disrotatory fashion, twisted at an angle of 52.9°. The distinction in relative dispositions is largely characterized by slip distance differences along both the long and short

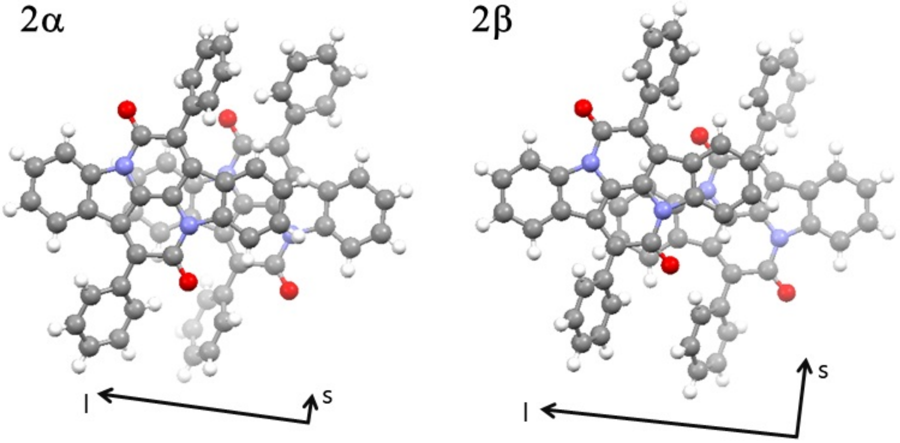

Figure 3. Closest slip-stacked molecular pairs extracted from unit cells of **2α** and **2β** crystals. Long (l) and short (s) axis slippage of the top molecule (shown darker) relative to the bottom molecule is depicted below the pairs.

molecular axes. Along the short axis direction *s*, a slip of 2.37 Å is observed for **2β** but only ~0.2 Å for **2α**. Along the long axis direction *l*, **2β** molecules are slipped by 5.90 Å while for **2α** the corresponding distance is 4.22 Å. The stacking distance between the almost planar molecular cores is 3.44 Å for **2α** and 3.54 Å for **2β**. Additional views of molecular packing are found in Figure S1.

Structure of Thin Films (TFs). Films of **2** prepared by thermal evaporation contained **2α**, **2β**, and amorphous phase (**2a**). Although the X-ray diffraction (XRD) patterns are sparse, it is apparent that the two crystalline TF polymorphs match the bulk forms of **2**, as seen in Figure S2. The films of **2α** have 2θ diffraction peaks at 7.5, 10.2, and 14.1°, corresponding to the (002), (10-1), and (111) diffraction planes, respectively (Figure S2). The films of **2β** show a characteristic 2θ diffraction peak at 10.0° from the (011) plane. A small amount of intensity around 7° and 14° suggests that these films contain some **2α**, too. Thermal evaporation at a deposition rate of 0.5 Å/s yielded predominantly **2β** films on substrates cooled to 80 K and predominantly **2α** films on substrates heated to 473K. Depositing **2** onto room temperature substrates at a rate of 10 Å/s yielded amorphous films **2a** until a certain thickness was achieved (> 100 nm), at which point **2β** layers began to crystallize. Upon annealing, either slowly at room temperature in air or rapidly on a hot plate, **2β** films convert to the **2α** form. Exposing a **2β** film to solvent vapors also induces annealing and reorganization to **2α**. Virgin **2α** TFs appear to gain crystallinity upon annealing, suggesting that they initially possess some amorphous regions. These observations lead us to conclude that all films are likely a mixture of at least two phases when initially deposited. Only thoroughly annealed films can be considered as purely **2α**.

Thin Film Composition from Polarized IR Reflectivity. Since amorphous **2a** and crystalline **2α** and **2β** are likely to have different SF properties, it was important to determine their relative amounts in the TFs. The ratio of **2α** and **2β** is readily established by XRD in the usual fashion. However, this method is blind to **2a**, and its fraction in the TFs was determined by IR reflectance in the carbonyl stretching region. The analysis follows an approach developed originally[39] for isotropic materials and later extended to anisotropic ones[40,41,42,43,44,45] and is described in detail in the Supporting Information. It takes advantage of the uniaxial nature of the sample (verified experimentally), approximates the dielectric constant at infinite frequency ε_∞ by its value in the visible,[45] and neglects polarization effects from diffuse scattering.[46]

Figure 5 shows the photomodulated infrared reflection-absorption (PM-IRRAS)[47]

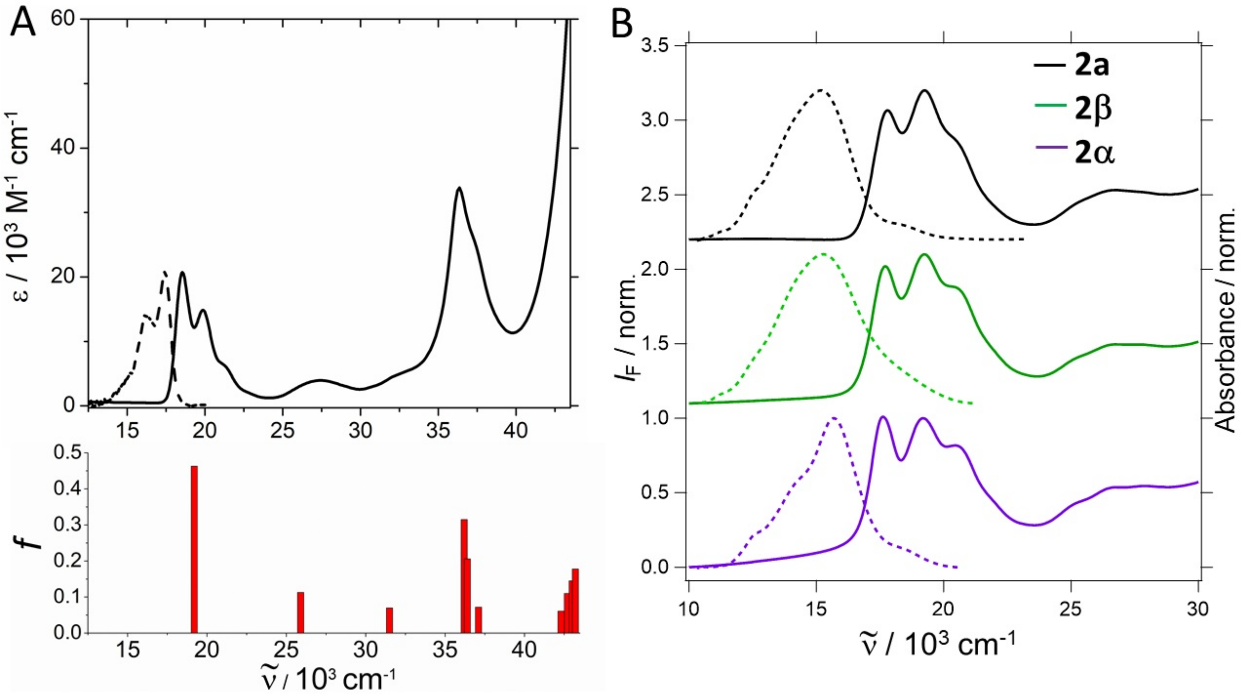

Figure 4. A: Absorption (solid) and fluorescence (dashed) spectra of toluene solution of **2**. The bar diagram shows results of a TD-DFT calculation (Table 2). B: Absorption (solid) and fluorescence (dashed) spectra of TFs of **2**.

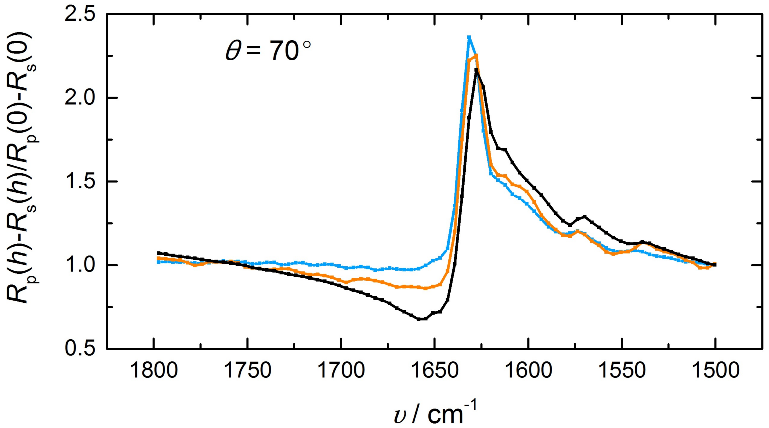

Figure 5. Normalized PM-IRRAS bands for amorphous (**2a**, blue), P2_1/n (**2α**, brown), and P2_1/c (**2β**, black) films in the regions of the carbonyl stretch at 1630 cm^{-1}.

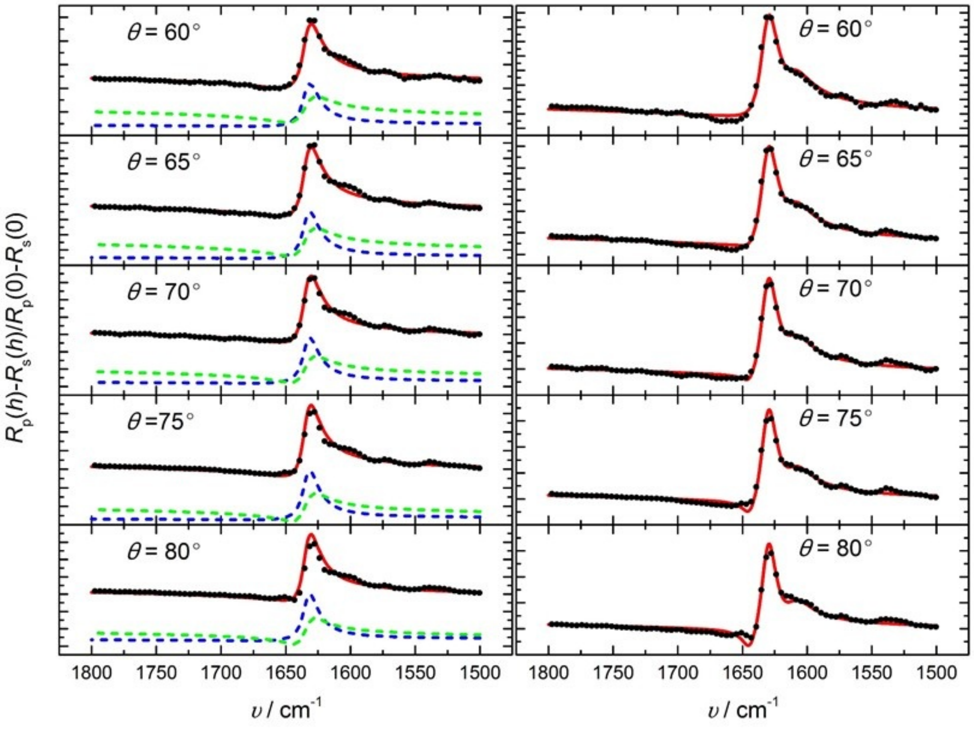

Figure 6. Fits to PM-IRRAS reflectances for a P2_1/c film using the island (left) and two-layer (right) models. Dotted blue and green curves show the crystalline and amorphous contributions to the total reflectance, respectively.

reflectance spectra of three different TFs of **2**. The carbonyl stretching band contains both absorptive and dispersive features and its position and lineshape differ among the samples. The complicated lineshape stems from the wavelength dependence of the optical constants in the vicinity of an optical transition (cf. Kramers-Kronig theory[48]). The optical constants for **2a** were obtained from a separate set of reflectance fits to data collected at eight different incidence angles θ from an 85 nm thick film of **2** that produced only a diffuse XRD pattern (Figure S3). These parameters were then used to globally fit the angle-dependent reflectances for the P2(1)/c (Figure 6) and P2(1)/n (Figure S4) 240 nm thick films that contain an unknown fraction of **2a**, using optical parameters for the crystalline contribution that are adjusted until the best fit is obtained (Figure S4), and using two different models for the internal structure of the TF (Figure 7). In the island growth model, pillars of either pure crystalline or pure amorphous material coexist side by side. In the two-layer model, an amorphous layer overlays a crystalline layer. The true structure is probably intermediate. The two models gave the same result, 25 - 26% of **2a**, both on a sample that was nominally **2α** and one that was nominally **2β** (in both cases to an extent of at least 80%).

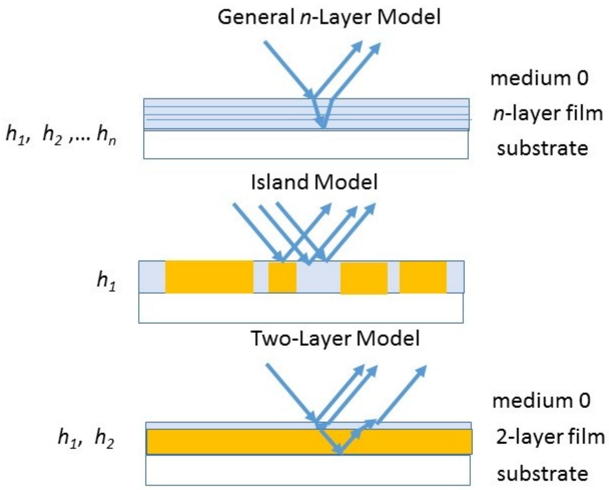

Figure 7. Thin film models. Top: General model. Center: Island model, with islands of equal thickness of amorphous and crystalline material. Bottom: Two-layer model with amorphous film as the upper layer.

Absorption and Emission Spectra. The absorption and fluorescence spectra of films and solutions of **2** are compared in Figure 4. The lowest energy peak in the vibrational envelope of the S_0 - S_1 transition in the absorption spectrum of **2** in toluene resides at 18 100 cm^{-1} ($\Delta E(S_1)$ = 2.24 eV) and is redshifted by about 450 cm^{-1} in the spectra of TFs ($\Delta E(S_1)$ = 2.19 eV). Fitting the absorption spectrum of **2** in solution with a Franck-Condon progression reveals a vibrational spacing $\tilde{\nu}$ = ~1350 cm^{-1} and a Huang-Rhys factor S of 0.7. Fitting the TF absorption spectra with this same functional form met with varying degrees of success. For **2α** the fit is poor, with S = 1.1, $\tilde{\nu}$ = 1 650 cm^{-1}, and $\tilde{\nu}_0$ = 17 540 cm^{-1} (2.17 eV). For **2β**, the fit is improved but far from satisfactory (S = 1.1, $\tilde{\nu}$ = 1 550 cm^{-1}, $\tilde{\nu}_0$ = 17 600 cm^{-1}, 2.18 eV). The red shift of the zerophonon energy, the poor fit to a pure Franck-Condon progression, and the abnormally large vibrational spacing compared with solutions are characteristics of increased Davydov interactions.

Bracketing of the triplet energy by sensitization with known triplet producers (Supporting Information) revealed the lowest triplet excitation energy $\Delta E(\mathrm{T}_1)$ of **2** in solution to be 1.27±0.05 eV. $\Delta E(\mathrm{T}_1)$ in thin films is not known but presumably changes little from that of solution. The shift of the $\Delta E(\mathrm{S}_1)$ value combined with the experimental $\Delta E(\mathrm{T}_1)$ value for **2** in solution suggests that $2\Delta E(\mathrm{T}_1) - \Delta E(\mathrm{S}_1) = 0.35$ eV.

Fluorescence of **2** in solution is red-shifted by about 1 000 cm^{-1} (0.12 eV) from its absorption and is a close mirror image of the absorption spectrum (Figure 4). Toluene solutions of **2** have ~80% fluorescence quantum yield, Φ_F. Fluorescence in TFs, however, is strongly quenched with Φ_F values less than 1%. Emission spectra for all TF samples are dominated by a broad feature centered near 15 000 cm^{-1} (1.86 eV), with some vibrational structure, best seen in **2α**. For TFs less than 100 nm thick, the amplitude ratio of the lowest energy vibronic absorption feature to the second vibronic absorption feature is higher for **2α** than for **2β**. The maxima of the fluorescence spectra of the three film types of **2** are red shifted from the absorption maximum by 2 000 - 2 500 cm^{-1} (0.25 - 0.30 eV).

Fluorescence decay of **2** in solution is monoexponential with a lifetime of 6 ns and does not change as a function of emission wavelength (Figure 8A). Unlike solution fluorescence decay kinetics, fluorescence decays collected on TFs are wavelength dependent, exhibiting multiexponential kinetics with time constants on the order of several tens of ps, 400 ps, and a small amplitude component of about 2 ns. The emission kinetics collected at 15 400 cm^{-1} (1.91

eV) is faster for **2α** than for **2β**. The relevant time constants of the individual decay components, their amplitudes, and Φ_F values can be found in Table S2. Emission decays of **2** TFs become significantly slower and approach monoexponential behavior as the red edge of the fluorescence is monitored (Figure S5), and this is most evident in the 12 500 cm^{-1} (1.55 eV) decay (Figure 8B). A global fit of a multiplex time-resolved fluorescence for a **2β** film reveals two separate emission bands with distinct exponential decay constants, (Figure 8C). The band associated with the slower time constant resembles the steady-state emission at room temperature. The emission gains strength and blue shifts as temperature is lowered (Figure 8D).

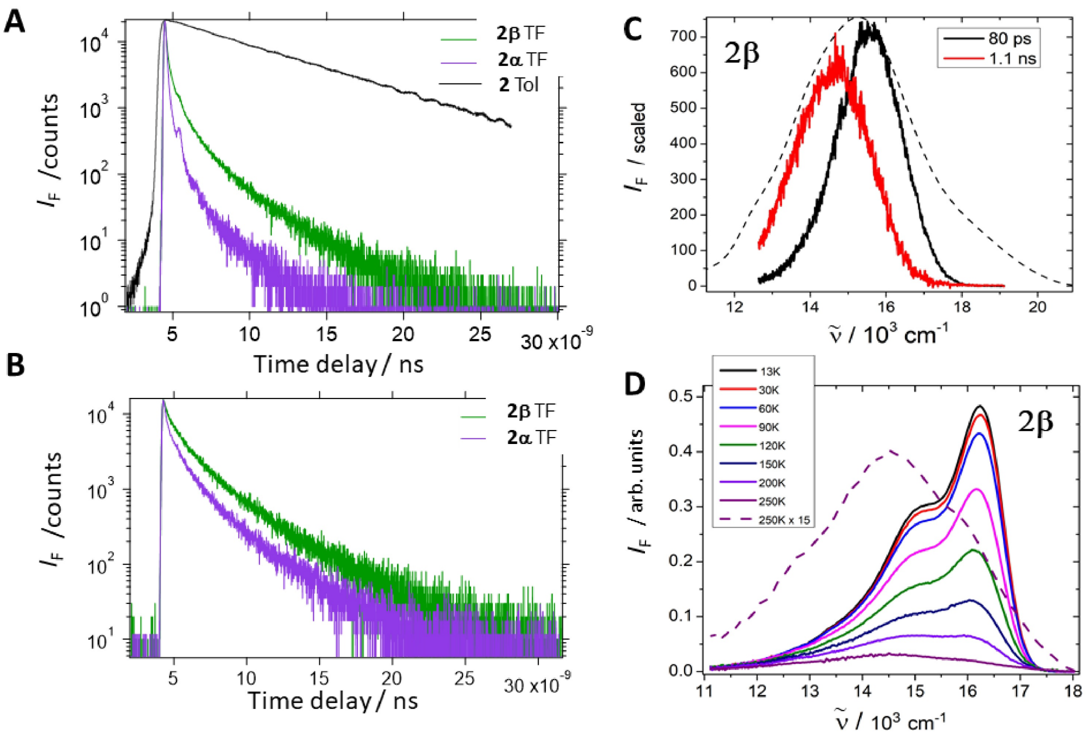

Figure 8. Time-resolved fluorescence collected at A: 16 000 cm^{-1} (1.98 eV), and B: 13 000 cm^{-1} (1.61 eV) for **2α** (purple) and **2β** (green) thin films. Black curve in A is fluorescence decay for **2** in toluene solution at 16 000 cm^{-1} (1.98 eV). C: Amplitude spectra from global fit of all emission wavelengths to biexponential decay function with 80 ps (black) and 1.1 ns (red) decay times. Dashed curve is steady-state fluorescence spectrum. D: Temperature dependence of steady-state emission spectrum for a **2β** film.

Transient Absorption. The raw transient absorption (TA) spectra of **2** in solution and in TFs are shown in Figure S6. In solution, they are dominated by singlet features until late times, when a T_1-T_n spectrum is revealed.[37] The ground state bleach and stimulated emission are found in positions expected from steady-state measurements while the S_1-S_n features are at 14 000 and 23 000 cm^{-1} (1.74 and 2.85 eV). Given the known solution triplet yield of Φ_T ~10%[37] and singlet lifetime of about 6 ns, the intersystem crossing time in an isolated molecule is estimated at 60 ns.

For all films the excited singlet populations, identified by the $S_1 \rightarrow S_n$ absorptions around 14 000 cm^{-1} (1.74 eV), decay largely within the first 10-50 ps (Figure 9A,C). Absorption features at 18 500 and 17 000 cm^{-1} (2.29 and 2.11 eV) are apparent after ~100 ps and persist for more than 5 ns. These features overlap with the ground state bleach that decays multiexponentially. The excited singlet decay is power dependent, and here we restrict our analysis to data from experiments using low fluence (~20 nJ/pulse, excitation density ~10^{18} cm^{-3}) to avoid the influence of singlet-singlet annihilation. At these low fluences, the kinetics of singlet decay and triplet rise are distinct for **2α** and **2β** films but are similar for **2a** and **2α**. The raw kinetics at representative wavenumbers are displayed in Figure 9B,D for comparison, where it is apparent that multiple species are contributing. A comparison between TA datasets at 77 and 298 K can be found in Figure S7. The temperature dependence is primarily characterized by a slowing of the decay of the spectral feature around 15 500 cm^{-1} (1.92 eV) and a concomitant extended rise of the long-lived feature at 17 000 cm^{-1} (2.11 eV), which mostly represents triplet population but begins at negative values due to overlap with stimulated emission.

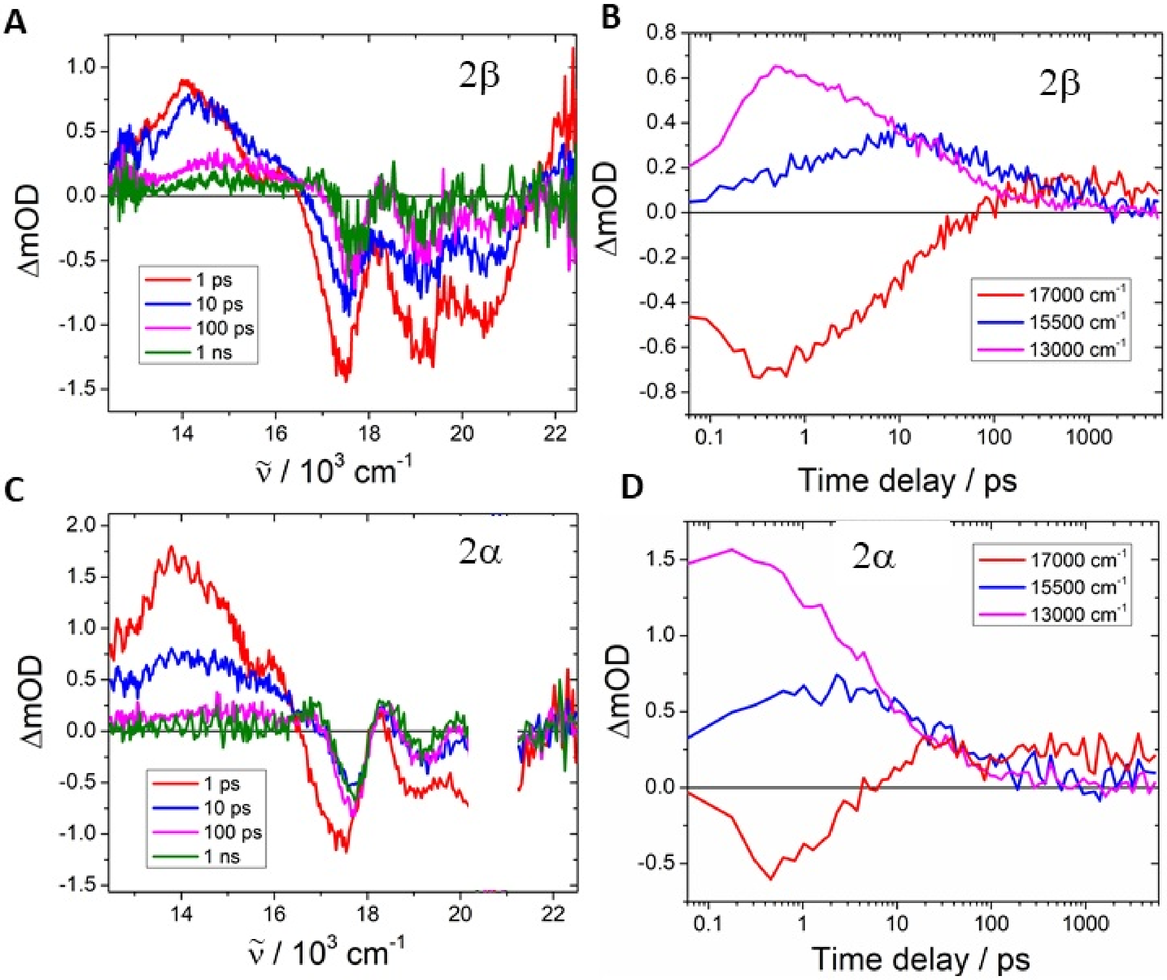

Figure 9. A, C: Selected spectra at delay times indicated in the legend for TFs of **2α** and **2β**. Data near 21 000 cm^{-1} (2.60 eV) are removed for the highly crystalline **2α** films due to intense pump scattering. B, D: Selected kinetic traces at positions roughly corresponding to singlet (magenta), triplet (red), and charge-transfer intermediate (blue) absorptions.

The TA data were interpreted with the aid of a global analysis fitting scheme for producing decay associated spectra and population decay profiles following an exponential decay model (Figures 10 and 11). The details of these fits can be found in the Supporting Information. The fitting procedure returned distinct spectra associated with three decay components, which are shown for a **2β** film in Figure 10A. The fast decaying (τ_1) feature is

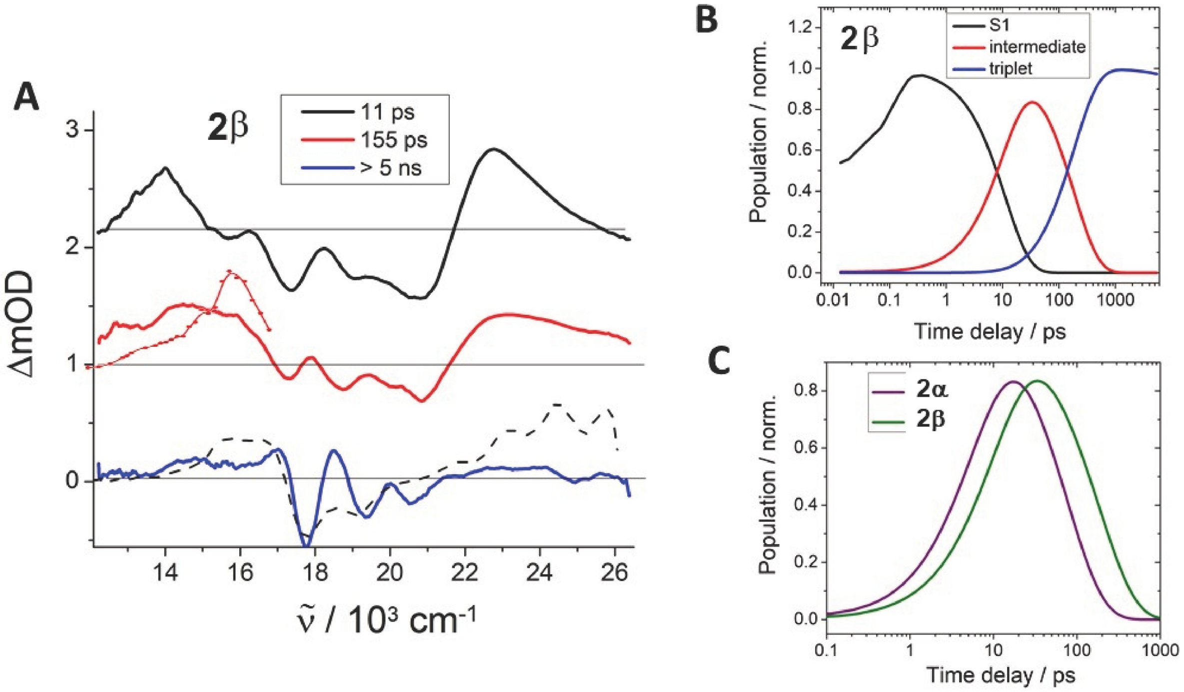

Figure 10. A: Decay associated spectra for a three-component exponential fit to transient absorption data for a **2β** film. Dashed black curve is the triplet/bleach spectrum of **2** in toluene collected from triplet sensitization. Red dots show the spectrum of radical cation from pulse radiolysis. B: Predicted population kinetics for **2β** film based on singular value decomposition (SVD) and global fit to data with sequential model. C: Intermediate population kinetics for **2α** (purple) and **2β** (green) films.

associated with the population in S_1 and the associated ground state bleach, S_1-S_n absorption, and stimulated emission. The longest lived (τ_3) feature is associated with a population in T_1 and the associated ground state bleach and T_1-T_n absorption. The features roughly match the triplet spectrum observed at long delay times in sensitized solutions of **2** (dashed curve in Figure 10A). The intermediate time (τ_2) spectrum overlaps with the fast and slow component spectra and also includes a unique absorption feature near 15 500 cm^{-1} (1.92 eV), very similar to the absorption peak of the radical cation of **2** at 16 000 cm^{-1} (1.98 eV, Figure S8), and a similar peak of the

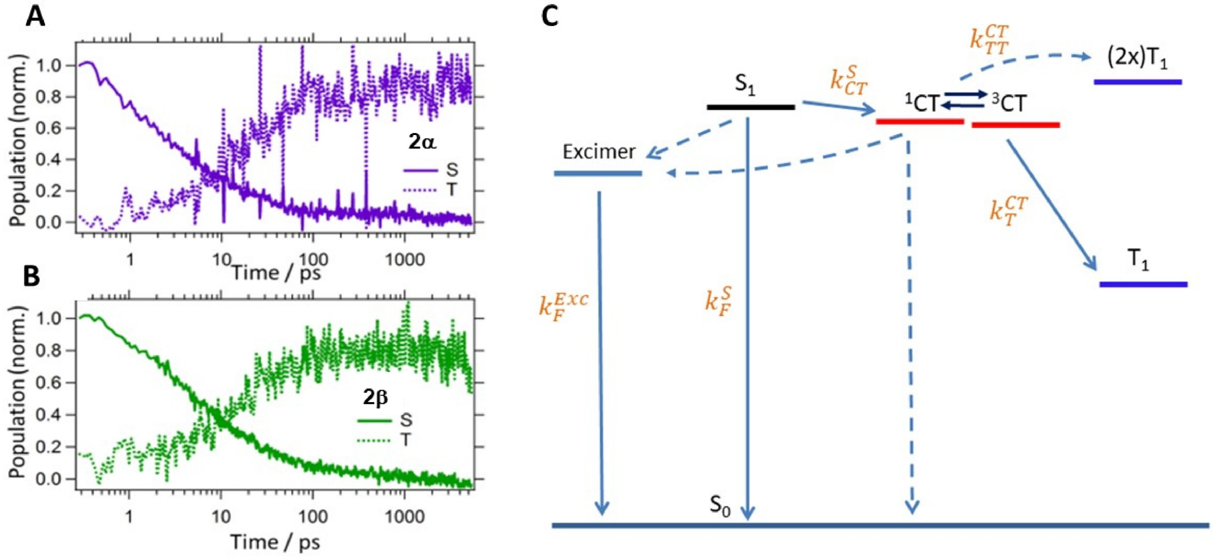

Figure 11. Singlet and triplet population kinetics generated from initial (singlet) and final (triplet) spectral analysis and global fit for A: **2α** and B: **2β**. C: Proposed kinetic scheme for population flow from S_1 after photoexcitation. Dashed curves are suggested routes not directly observed experimentally.

radical anion at the same location,[37] which makes it very likely that the intermediate is a radical cation - radical anion pair. We assign the species S_1, T_1, and the charge-transfer intermediate to the component spectra and plot their evolution in Figure 10B. A summary of fitted time constants for solution and films can be found in Table 1. The most notable distinction between **2α** and **2β** films is the faster loss of the population of S_1 and of the intermediate in the former (Figure 10C).

The singlet decay kinetics of transient absorption for **2a** TFs most resembles that of **2α** TFs. However, the stimulated emission near 20 000 cm^{-1} (2.48 eV) is largely suppressed, and the spectra are instead dominated by a broad absorption at 19 000 – 22 000 cm^{-1} (2.36 - 2.73 eV). In addition, the region near 16 500 cm^{-1} (2.05 eV) features a bleach rather than the photoinduced absorption that is present in the polycrystalline films.

Triplet Yield. In order to determine Φ_T from the TA data, the triplet absorption strength at 5 ns delay and 16 700 cm^{-1} (2.07 eV) was compared to the initial ground state bleach at 1 ps and 17 900 cm^{-1} (2.22 eV). This ratio was scaled by the known extinction coefficients for the species at these wavenumbers[37] (Table 1). However, in order to quantify Φ_T for a film whose molecules may be partially aligned due to the proximity of substrate surface, we need to ask whether bleach and triplet transition dipole moments are aligned parallel and if not, perform appropriate corrections.

Correction for Partial Alignment. It is fairly common in SF studies to find that molecules in TFs are partially aligned, typically in a fashion that is uniaxial relative to surface normal.[49] Partial alignment is revealed by measurement of the dependence of polarized spectral intensity on the angle of incidence. It requires the relation between the absorbances due to the ground state and those due to a transient such as a triplet or a charge-transfer state to be modified from that which applies in an isotropic solution, unless the transitions involved have parallel polarizations.

The Supporting Information provides a derivation of a simple approximate procedure that provides the correction factor needed for the conversion of absorbance ratios $E^{\alpha}{}_{p}{}^{\omega}(\nu)/E^{\beta}{}_{p}{}^{\omega}(\nu)$ or $E^{\alpha}{}_{s}{}^{\omega}(\nu)/E^{\beta}{}_{s}{}^{\omega}(\nu)$, measured on the TF at angle of incidence ω, with light polarized parallel (s) or perpendicular (p) to the plane of incidence, into absorbance ratios $E^{\alpha}{}_{\mathrm{iso}}(\nu)/E^{\beta}{}_{\mathrm{iso}}(\nu)$ that would be observed if the solution were isotropic and that are equal to the sought ratios of products of extinction coefficients and concentrations, $\varepsilon^{\alpha}(\nu)c^{\alpha}/\varepsilon^{\beta}(\nu)c^{\beta}$. Here, α and β label two transitions under observation, with transition moments at angles α and β with the molecular orientation axis, respectively, and $E_{\mathrm{iso}}(\nu)$ is absorbance as a function of frequency measured on an isotropic sample, which is independent of light polarization and angle of incidence.

The relation is

$$[E^{\alpha}{}_{p}{}^{\omega}(\nu)/E^{\beta}{}_{p}{}^{\omega}(\nu)] = [E^{\alpha}{}_{\mathrm{iso}}(\nu)/E^{\beta}{}_{\mathrm{iso}}(\nu)][(1 - 3\sin^2\omega - d^{\beta\omega})/(1 - 3\sin^2\omega - d^{\alpha\omega})]$$

$$[E^{\alpha}{}_{s}{}^{\omega}(\nu)/E^{\beta}{}_{s}{}^{\omega}(\nu)] = [E^{\alpha}{}_{p}{}^{\omega}(\nu)/E^{\beta}{}_{p}{}^{\omega}(\nu)](d^{\alpha\omega}/d^{\beta\omega}),$$

where $d^{\alpha\omega} = E^{\alpha}{}_{s}{}^{\omega}(\nu)/E^{\alpha}{}_{p}{}^{\omega}(\nu)$ and $d^{\beta\omega} = E^{\beta}{}_{s}{}^{\omega}(\nu)/E^{\beta}{}_{p}{}^{\omega}(\nu)$.

The requisite molecular transition polarization directions α and β can often be obtained from measurements on partially oriented samples (e.g., linear dichroism in stretched polymers or liquid crystals), relatively easily for transitions from the ground state[50] and with more difficulty for transitions from short-lived states such as triplets.[51] Transition moment directions for charge-transfer states need to be obtained from similar measurements on the radical cation or radical anion. It is nowadays easy to calculate all of these polarization directions using the TD-DFT method, but little is known about the reliability of the results for molecules of low symmetry, in which these directions are not constrained to molecular symmetry axes.

Table 1. Triplet Yield and Time Constants for Population Evolution Derived from Global Fitting of Transient Absorption Data.

	τ_1/ps	Φ_{CT} (%)	τ_2/ps	Φ_{T} (%)	τ_3/ns
2 in benzene[a]	~6×10^4	-	-	4 ± 2	1.5×10^5
2α TF[a]	6.2	31 ± 4	74	23 ± 6	103 ± 8
2β TF uncorr.[b]	11	[34 ± 4]	155	[40 ± 7]	205 ± 12
2β TF corr.[c]	11	**40 ± 10**	155	**60 ± 17**	205 ± 12
2a TF[a]	8	21 ± 4	112	17 ± 2	123 ± 10

[a] No discernible alignment effect. [b] Without correction for alignment effect. [c] Corrected for

alignment effect.

Corrections of the yields of the triplet and of the charge-transfer state for possible partial alignment in our uniaxial TF samples (Table 1) are expected to be small, since all the relevant transitions are computed to be polarized in similar directions. They are based on polarized measurements at several angles of incidence (Tables S3 and S4, cf. plots in Figure S9) and on TD-DFT B3LYP/6-311+G* calculated angles between polarization directions, measured counterclockwise from the direction of the central C=C bond (Tables 2 and S9 - S11). Computations for the conrotatory and disrotatory conformers of **2** gave almost identical results (Tables S12 and S13). As seen in Figure 4A and Tables 2, S9, and S10, the agreement of calculated with observed excitation energies and intensities is excellent. Nevertheless, one could doubt the reliability of the calculated transition moment directions.

In order to test the sensitivity of the calculated polarization directions to minor changes in the method of calculation, we recalculated them with the same functional and basis set but in the Tamm-Dancoff approximation (TDA).[52] The two sets of results are compared in Tables 2, S9 - S11, and in more detail in Tables S12 and S13. The low-energy excited states obtained in two the sets of calculations are in a one-to-one correspondence up to about 35 000 cm^{-1} (4.34 eV) for S_0 - S_n, about 32 000 cm^{-1} (3.97 eV) for T_1 - T_n transitions, and up to ~30 000 cm^{-1} (3.72 eV) for D_0 - D_n transitions in the radical ions. Within these ranges, the polarization directions of strong transitions obtained by the two methods agree within a few degrees. The agreement is only within 10 to 20 degrees for many of the weak transitions, not observable for transients in our experiments. At higher energies, there is no simple correspondence between transitions calculated by the two methods.

For the intense transitions relevant for the interpretation of our experiments the calculated polarization directions appear trustworthy. These transitions are (i) S_0-S_1 in **2**, observed as bleach at ~18 600 cm^{-1} (2.31 eV) (Figure 10) and calculated (Table 2) at 19 200 cm^{-1} (2.38 eV), polarized at ~65°, (ii) transition T_1-T_7 in **2**, observed at ~16 700 cm^{-1} (2.07 eV, Figure 10, cf. Figure 4) and calculated (Table S9) at 17 600 cm^{-1} (2.18 eV), polarized at ~54°, (iii) transition D_0-D_6 in **2**$^{\bullet+}$, observed at ~15 500 (1.92 eV, Figure S8) and calculated (Table S10) at 15 300 cm^{-1} (1.90 eV), polarized at ~60°, (iv) transition D_0-D_2 in **2**$^{\bullet-}$, also observed[37] at ~15 500 cm^{-1} (1.92 eV) and calculated (Table S11) at 15 500 cm^{-1} (1.92 eV), polarized at 56°. Transitions D_0-D_6 in **2**$^{\bullet+}$ and D_0-D_2 in **2**$^{\bullet-}$ overlap and are calculated to have virtually identical transition energies, intensities, and polarizations. They will be handled jointly as a transition characterizing the CT state and polarized at ~58°. Approximately half of the observed intensity is to be assigned to each of the two transitions.

Table 2. Absorption Spectrum of **2** and Calculated Allowed Excitations from the S_0 State of Centrosymmetric **2** (conrotatory Ph groups, as in **2α**).[a]

State no.[b]	Observed		Calculated			
	$\Delta E/10^3$ cm^{-1} [c]	*f* [d]	$\Delta E/10^3$ cm^{-1} [e]	*f* [d]	α/deg [f]	α/deg [g]
1	18.6	0.22	19.2	0.461	65.0	64.6
3	27.2	0.05	25.9	0.113	−55.8	-58.3
6			27.4	0.002	−49.2	-35.6

9			30.1	0.004	29.8	16.4
10			30.9	0.020	42.5	31.7
11	32.3	0.04	31.5	0.070	−28.1	-34.2
13			33.5	0.008	60.9	62.8
15	36.4	0.37	36.2	0.305	−28.5	-89.2
16			36.4	0.217	1.2	-23.1
18	37.3	0.11	37.1	0.072	10.8	-4.9
21			39.4	0.018	14.9	22.6
22			39.6	0.004	−19.9	-0.2
23			39.8	0.006	−3.0	2.2
27			41.3	0.005	77.4	80.8
29			42.2	0.008	32.6	40.7
30	~43		42.3	0.059	39.7	53.9
32			42.7	0.107	22.8	23.0
34			43.0	0.140	14.4	
36			43.2	0.187	26.2	
38			43.8	0.149	−75.7	
39			43.9	0.137	1.7	
40			43.9	0.086	−86.1	
45			44.6	0.078	−30.6	
47			45.0	0.002	75.1	

[a] TD-DFT B3LYP/6-311+G*//B3LYP/6-311+G*, *E* = -1490.5751663 a.u. The calculated results for the conformer with disrotatory twist of the phenyl groups as in **2β**, *E* = -1490.575518 a.u., are very similar and the excitation energies differ at most by 200 cm^{-1} (see Tables S12 and S13). Both conformers are probably present in similar amounts in solution. [b] All calculated transitions are numbered sequentially, but only those with non-zero oscillator strength are listed.

For a full list, see Tables S12 and S13. [c] Absorption peaks in toluene solution. [d] Oscillator strength. [e] Excitation energy in vacuum. [f] Transition moment direction measured counterclockwise from the central C=C axis in formula **2** (Figure 2). [g] The same as footnote *f*, but the calculation used the TDA approximation.

No evidence for partial alignment is observed for **2a** and **2α**, where amplitude ratios are independent of the angle of incidence. Their Φ_{T} and Φ_{CT} values do not need to be corrected. Figure S10A shows that in contrast, as the tilt angle is increased, the bleach and triplet TA amplitudes in **2β** change: the former decreases and the latter increases. As a result, the amplitude ratios $E^{\mathrm{T}}{}_{p}{}^{\omega}(\nu)/E^{\mathrm{S}}{}_{p}{}^{\omega}(\nu)$ (Figure S10B) and $E^{\mathrm{CT}}{}_{p}{}^{\omega}(\nu)/E^{\mathrm{S}}{}_{p}{}^{\omega}(\nu)$ (Figure S11), which in **2α** remain constant, in **2β** grow with increasing ω. The corrected results for both Φ_{T} and Φ_{CT} of **2β** are shown in bold in Table 1. The correction is small, because the polarization directions for the spectral transition from S_0 and from the transients T_1 and D_0 do not differ much. The different behavior of **2α** and **2β** TFs may be related to the presence of multiple crystallite orientations in the former, which exhibit peaks arising from multiple crystal facets in the powder XRD pattern (Figure S2).

Prediction of Better Packing Geometries. The formation of excimers and charge-transfer species upon excitation of **2** suggests that these processes outcompete SF. Since **2** has many attractive properties, it seemed worthwhile to determine whether a better molecular packing might suppress these undesirable processes and enhance the rate of SF. Once desirable packing structures are known, they could be approached by modifying the molecular structure or by synthesizing a covalent dimer with a favorable structure.

In order to find out what more desirable pair structures might look like, we used the recently developed computer program "Simple", described in detail elsewhere[24,53] (earlier versions with additional detail are also available[8,22]). This freely available program applies the Fermi Golden Rule to SF in the diabatic framework and pairwise approximation, in which many-body effects are neglected. It identifies all local maxima of the rate of conversion of a singlet exciton to a "double triplet" biexciton in a molecular pair as a function of the six degrees of freedom available for the description of the mutual disposition of two rigid bodies. The hard-sphere model is used to avoid unphysical geometries in which the two molecules would interpenetrate. At first, a series of approximations within the frontier orbital model is adopted to compute the square of the electronic matrix element rapidly for a grid of billions of geometries and to identify its local maxima. This search yields a set of dozens or hundreds of preliminary geometries as starting points for further refinement that maximizes the sum of contributions from Boltzmann-weighted relative SF rate constants from the two lowest exciton states S* and S**, estimated using Marcus theory. According to the experience gathered so far, this refinement typically produces between a few and a few hundred favored geometries as the main product of the effort.[24,53,54] At these geometries, the contributions of intermolecular interactions to the energy balance of exciton formation and the energy balance of the SF process, as well as the biexciton binding energy, are also evaluated. It appears just as important to avoid a large Davydov splitting, which generally induces unfavorable SF energy balance, as it is to reach a high value of the electronic matrix element.

We emphasize that the primary purpose of the program is not the evaluation of absolute or even relative rates of SF as a function of pair geometry, but the identification and approximate ranking of those geometries that are likely to be particularly advantageous for SF and the detection of associated structural motifs. It is anticipated that more accurate calculations could ultimately use these geometries as starting points. The shortcomings of the model and the justification of the various neglects are discussed elsewhere.[24,53] Here, we only note the most serious aspects that may limit the utility of the program: (i) the two-body approximation and (ii) the absence of even only approximate evaluation of the rates of competing decay processes, without which triplet yields cannot be estimated. These undesirable decay processes may intervene at the level of the original singlet exciton and prevent its conversion to a biexciton (formation of an excimer or a charge-separated state, too stabilized to be capable of producing two triplet excitons, or internal conversion to the ground state of the original molecule or a photoproduct). They may also intervene at the level of the biexciton, interfering with its dissociation to two triplet excitons (decay of the biexciton to a combination of a triplet and a ground-state molecule, or to two ground-state molecules). All the method provides is an estimate of the driving force for the generation of an excimer or a CT state.

Comparison with ab Initio Computations. Since the evaluation of the electronic matrix elements and of the Davydov splitting using Procedure III in the Simple program involves a series of approximations, it is important to check the results against those of a more accurate method. We have chosen the ab initio Frenkel Davydov exciton model (AIFDEM) procedure[38] for the purpose, and describe it in detail in the Supporting Information. The ab initio calculation is quite laborious and for molecules as large as **2** such comparisons can only be made at a relatively small number of pair geometries. Since we are only interested in the performance of the Simple procedure at geometries where SF is predicted to be fast, we have chosen the first 48 best pair geometries that maximize $(T^A)^2$ as identified by the Simple program, using the 6-311+G basis set. Figure 12A compares the results for the sum of the squares of the electronic matrix elements connecting the lower and the upper exciton states S* and S** to the biexciton ^{1}TT*, and Figure 12B similarly compares the computed magnitude of the energy difference between S* and S** (the Davydov splitting). Both comparisons are qualitatively satisfactory and suggest that the results of the Simple procedure are meaningful.

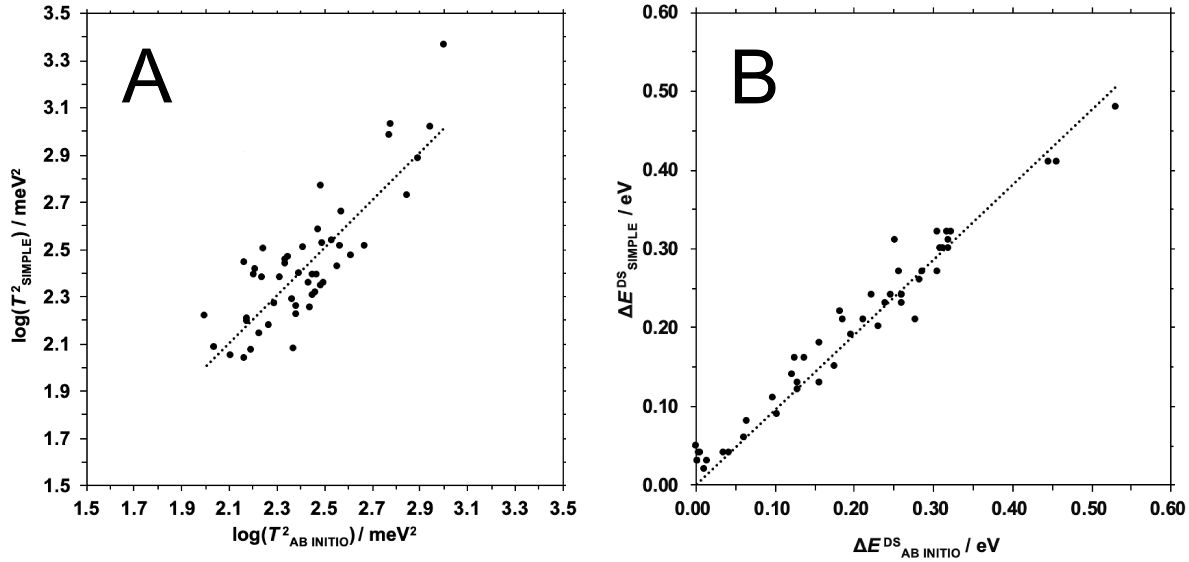

Figure 12. The correlation of A: T^2 and B: the Davydov splitting $\triangle E_{\mathrm{DS}}$ calculated by Procedure III and by the ab initio Frenkel-Davydov Exciton Model. Correlation coefficients: A, $R^2 = 0.70$; B, $R^2 = 0.95$.

Optimal Pair Geometries for 2. Results obtained for the 20 pair structures of **2** that have the highest relative SF rate constants k_{SF} predicted by Procedure III of program Simple are collected in Table 3. The first eight pair structures are visualized in Figure 13. Subsequent 12 structures are shown in Figures S12 - S14 of the Supporting Information, which also provides a brief description of the computational procedure and contains leading references to a full detailed description. For comparison, results calculated for the highest k_{SF}/k_0 value pair structures actually found in the crystals of **2α** and **2β** and shown in Figure 3 are included.

Table 3. Results from Procedure III of program Simple for the first 20 pair structures of **2** optimized for the largest relative SF rate constant k_{SF}, compared with real pair structures from crystals of **2α** and **2β** (energy in meV).[a]

No.	$\lvert T^*\rvert$[b]	$\lvert T^{**}\rvert$[c]	T^2 [d]	$4\lvert(h_A l_A \vert h_B l_B)\rvert$[e]	ΔE_{DS}[f]	$\Delta E(S^*)$[g]	$\Delta E(S^{**})$[h]	ΔE_{BB}[i]	k_{SF}/k_0[j]
1	6.14	0.00	37.65	24	9	6	−4	10	1.00
2[k]	1.35	5.55	32.63	24	23	10	−13	6	0.63
3	4.35	0.00	18.88	5	9	8	−1	2	0.48
4	2.81	2.98	16.76	6	0	0	0	5	0.42
5	3.52	1.07	13.53	49	52	21	−31	6	0.37
6	3.61	0.07	13.03	50	54	24	−30	5	0.35
7[l]	6.78	0	46	163	165	82	−84	7	0.35
8	2.93	0.00	8.60	24	24	−4	−29	17	0.34
9	3.33	0.31	11.20	38	40	17	−23	5	0.33
10	3.31	0.45	11.17	50	53	24	−29	4	0.30
11[m]	5.18	0.67	27.28	138	138	68	−71	6	0.29
12	2.68	1.68	10.03	4	4	−3	−8	7	0.28
13	3.20	0.94	11.13	61	63	28	−35	5	0.27
14	2.86	1.28	9.82	18	21	10	−12	3	0.27
15	2.73	1.57	9.94	28	29	12	−17	4	0.26
16	3.47	0.03	12.02	80	83	39	−44	4	0.26
17	2.99	1.72	11.87	67	67	29	−37	6	0.25
18	3.30	0.14	10.91	76	78	36	−42	4	0.25
19	2.57	2.28	11.77	51	50	21	−29	6	0.24

20	0.89	2.90	9.21	12	12	1	−11	7	0.23
2α	3.72	0.00	13.81	87	349	175	-175	3	0.006
2β	4.99	0.00	24.88	71	294	149	-145	3	0.026

[a] 6-311G basis set, reorganization energy $\lambda = 0.22$ eV. [b] Electronic coupling elements from the lower excitonic state S*. [c] Electronic coupling elements from the upper excitonic state S**. [d] $T^2 = (T^*)^2 + (T^{**})^2$. [e] First approximation to the Davydov splitting (excitonic transition density - transition density interaction only, evaluated in the point-charge approximation). [f] Absolute value of the energy difference between S* and S** states (Davydov splitting). [g] SF energy balance from

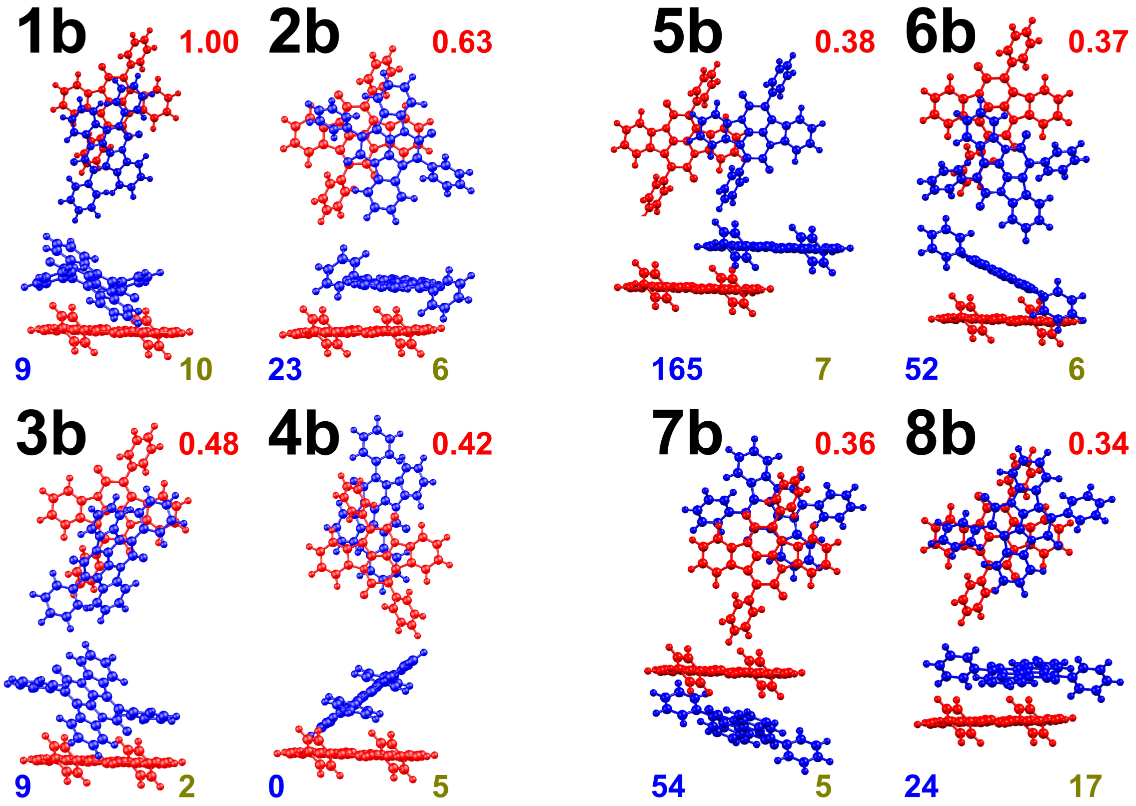

Figure 13. Calculations by Procedure III of program Simple. The first eight pair structures of **2** with the largest rates k_{SF}^{rel} relative to the best structure (red), calculated Davydov splitting (blue), and $^1(T_1T_1)$ biexciton binding energy (yellow), both in meV. The absolute rate calculated for structure 1b is $k_{SF} = 8.4\times10^{10}$ s^{-1}.

the S* state, $E(T_1T_1) - E(S^*)$. [h] SF energy balance from the S** state. [i] Biexciton binding energy. [j] Relative SF rate constant; $k_0 = 8.4\times10^{10}$ s^{-1}. [k] This structure is very similar to structure no. 11 in Table 4. [l] This structure is very similar to structure no. 10 in Table 4. [m] This structure is very similar to structure no. 15 in Table 4.

Results obtained for the 20 pair structures of **2** with the largest SF matrix element $|T^A|^2$ predicted by Procedure I of program Simple are given in Table 4. The first 12 pair structures are visualized in Figure 14, where the magnitude of the Davydov splitting and the biexciton binding energies obtained by Procedure III are also listed. Subsequent eight structures are shown in Figures S15 and S16 of the Supporting Information, along with a brief description of the computational procedure and references to full detailed description.

Table 4. Results from Procedures I and III of program Simple for the first 20 pair structures of **2** optimized for the largest square of the SF coupling element $|T^A|^2$ (energy in meV).[a]

No.	$\|T^A\|$ [b]	$\|T^B\|$ [c]	$(T^A)^2$	$(T^B)^2$	$\|4(h_Al_A\|h_Bl_B)\|$ [d]	ΔE_{DS} [e]	ΔE_{BB} [f]
1	9.31	1.29	86.71	1.66	333	328	16
2	8.77	4.04	76.94	16.29	288	291	15
3	8.24	7.44	67.87	55.32	350	344	21
4	8.05	8.04	64.74	64.64	434	457	4
5	7.68	7.70	58.95	59.31	354	346	18
6	7.11	4.92	50.53	24.17	296	292	10
7	6.50	0.82	42.22	0.67	288	285	8
8	6.27	1.73	39.36	3.00	184	191	7

9	5.56	2.94	30.90	8.62	304	305	5
10[g]	5.32	5.08	28.34	25.80	165	168	7
11[h]	5.04	3.23	25.40	10.42	29	27	7
12	4.92	7.20	24.24	51.89	265	258	9
13	4.76	7.24	22.67	52.41	272	272	12
14	4.67	1.21	21.83	1.46	14	3	8
15[i]	4.41	3.40	19.43	11.58	138	138	6
16	4.38	3.77	19.17	14.18	422	430	3
17	4.06	1.18	16.49	1.39	366	371	3
18	3.96	1.22	15.68	1.48	191	194	5
19	3.91	3.77	15.33	14.22	132	136	8
20	3.84	4.29	14.75	18.39	275	279	5

[a] 6-311G basis set. Highlighted rows identify similar structures found for optimization of k_{SF} in Table 3 and $|T^A|^2$ in Table 4. [b] Electronic coupling elements for initial excitation on partner A from Procedure I. [c] Electronic coupling elements for initial excitation on partner B from Procedure I. [d] First approximation to the Davydov splitting (excitonic transition density - transition density interaction only, evaluated in the point-charge approximation) from Procedure III. [e] Absolute value of the energy difference between the lower S* and upper S** excitonic states (Davydov splitting) from Procedure III. [f] Biexciton binding energy from Procedure III. [g] This structure is very similar to structure no. 2 in Table 3. [h] This structure is very similar to structure no. 7 in Table 3. [i] This structure is very similar to structure no. 11 in Table 3.

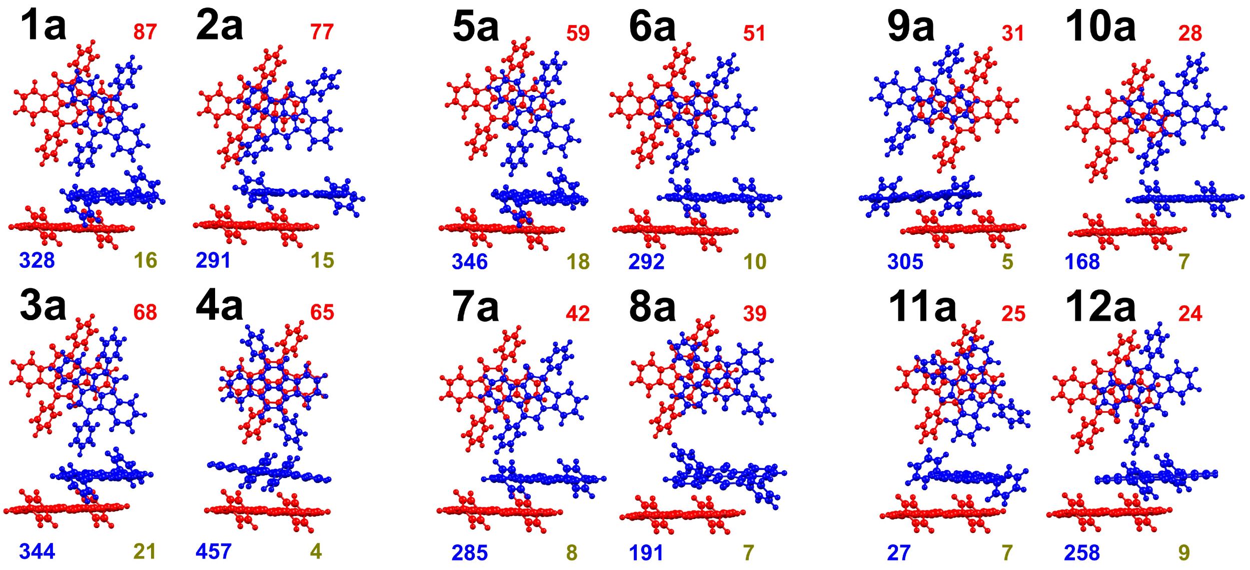

Figure 14. Calculations by program Simple. The first 12 pair structures of **2** with the largest $|T^A|^2$ (from Procedure I, in meV^2, red), Davydov splitting (blue), and biexciton binding energy (gold), both from Procedure III (in meV).

Discussion

Photophysics of 2a, 2α, and 2β. A rough picture of triplet population kinetics can be gleaned from TA traces extracted at 16 700 cm^{-1} (2.07 eV, Figure 9B,D), but congestion from overlap of the spectra of multiple photoexcited species precludes a quantitative analysis. Therefore, an analysis that tracks the triplet (i.e., longest-lived) and excited singlet (i.e., shortest-lived) populations was performed to monitor their evolution (Figure 11AB and Figure S9). This method suppresses the influence of minority species and spectral shifting, and in other SF systems (e.g., tetracene[55]) has produced a clear one-to-two evolution from S_1 to T_1. The lack of such a relationship, specifically the faster decay of S_1 compared with the rise of T_1, implicates a more complicated scheme here. A species that forms directly from S_1 in less than 20 ps and decays in less than 200 ps is found in the transient absorption spectra and must be included to properly fit the population evolution. We propose the scheme shown in Figure 11C, which includes a branching of decay pathways, and tentatively assign the intermediate as a species with CT character, consisting of a radical cation $\mathbf{2}^{\bullet+}$ and a radical anion $\mathbf{2}^{\bullet-}$. This assignment is supported by the rough match between the observed spectrum of the intermediate (Figure 10A) and those of $\mathbf{2}^{\bullet+}$ (Figure S8) and $\mathbf{2}^{\bullet-}$.[37] In the spectral range probed here, the observed and the calculated absorption peaks of $\mathbf{2}^{\bullet+}$ and $\mathbf{2}^{\bullet-}$ overlap essentially perfectly. Other interpretations of this intermediate are possible (e.g., a bound ^{1}(TT) species) but remain entirely speculative.

The inclusion of the excimer loss pathway in the scheme shown in Figure 11C is supported by time-resolved fluorescence experiments that reveal a red-shifted emission that persists with a 1.1 ns lifetime, well beyond the 80 ps lifetime of S_1 fluorescence in the solid (Figure 8C). The excimer is assumed to be at lower energy than S_1 and to undergo radiative and nonradiative decay to the ground state. Its formation is apparently thermally activated, as the steady-state emission becomes more monomer-like as temperature is lowered (Figure 8D). Absorption by the excimer is not obvious in the TA data, preventing a determination of its quantum yield. It may broadly underlie the intermediate and triplet spectra.

The faster evolution of S_1 into the CT state for **2α** compared with **2β** TF (Figure 10C) is noteworthy and may be related to the slightly closer intermolecular distance present in the unit cell. The direct formation of triplets from the CT state, and not clearly from the excimer, suggests that the excimer provides a competitive decay pathway and may be formed from S_1 or by charge recombination from CT.[56] The lower yield of the CT state in **2α** despite its faster formation rate constant suggests that the alternate pathway directly from S_1 to the excimer is accelerated in **2α** films and may arise from the smaller degree of slipping in the π-stacked neighbors in the unit cell of **2α** compared with **2β**.

The somewhat reduced CT state yield for **2a** films suggests that amorphous character supports fast formation of excimers from S_1 (the pathway to the left in Figure 11C) rather than the route through the CT state. The lower yield of triplets further supports the notion of the excimer as a trap state rather than a facilitator of triplet formation, which is consistent with our prior work on engineered films of 1,3-diphenylisobenzofuran.[57] The small but nonzero triplet yield in **2a** is not surprising given the likelihood of small crystalline domains not detectable by XRD that produce triplets with yields similar to the **2α** or **2β** forms.

The presence of excimer formation pathways has previously been implicated as deleterious in endothermic SF situations.[57,58] Excimer formation is less likely at low temperature, which is evident from the structured fluorescence and the slowing of the CT decay, from which at least a portion of the excimers arise (Figure S7). The CT yield can be determined with the aid of the known radical cation extinction coefficients (Figure S8) to be roughly 20% for **2a**, 30% for **2α** and 40% for **2β** at room temperature. We propose that from the CT intermediate, branching of decay pathways produces excimers, triplets, and possibly also ground state molecules, resulting in the yields shown in Table 1. The lower Φ_T compared with Φ_{CT} in all cases suggests that the excimer formation pathway from CT funnels population away from the triplet pathway, and it is difficult to evaluate if two triplets form from CT (as in SF), or just one (as in intersystem crossing). We cannot be sure but consider the latter more probable, because SF from the CT state would be at least as endoergic as the unobserved SF from the initial singlet exciton, whereas ISC in the CT state must be nearly isoergic. Processes in which a real CT state mediates triplet formation have been observed in other solid-state molecular systems[59]and dimers.[60,61] In the first of these, SF has been implicated, but additional work is needed to determine the formation mechanism of most of these triplets.

A different conclusion has been reached in very recent study by Fallon et al.[62] of a group of solids whose molecular structures are nearly identical with that of **2** (they carry alkylthienyl instead of phenyl substituents), and this might be viewed as a discrepancy. Tacitly assuming that thin films of these materials are isotropic or that the observed singlet-singlet and triplet-triplet transition moments are parallel, the authors used transient absorption measurements to find a triplet yield of ~60% at 1 ns after initial excitation (in the absence of a kinetic analysis, the initial yield remains unknown). Time-resolved EPR measurements did not reveal quintet signals, which would provide positive evidence for SF. However, triplets were observed and their spin polarization was *AEEAAE* (low to high magnetic field), compatible with SF and different from the *EEEAAA* polarization observed for triplets formed by intramolecular ISC in molecules isolated in rigid solution. The authors noted the high speed with which the observed triplets are formed and concluded that they originate in SF. However, it seems to us that they are equally likely to originate in ISC in the CT state. This process can also be very fast and would also yield triplets with the observed spin polarization pattern.[63,64] Thus, there possibly is no discrepancy between the results for the two similar groups of compounds, after all. Our efforts to observe time-resolved EPR signals for **2** failed due to very poor signal-to-noise ratios.

In support of their claim of SF in their variously substituted thienyl analogs of **2**, the authors quote results of DFT calculations of the relative size of $\Delta E(T_1)$ and $\Delta E(S_1)$, acknowledging that they will be modified in the solid.[62] The computational results are systematically biased in favor of SF by the authors' choice to use vertical excitation energies for $\Delta E(S_1)$ and adiabatic excitation energies for $\Delta E(T_1)$. For illustration, consider the results for isolated **2** at the B3LYP/6-

311G level: for $\Delta E(\mathrm{S}_1)$, the adiabatic value is 2.31 and the vertical, 2.42 eV, and for $\Delta E(\mathrm{T}_1)$, the values are 1.20 and 1.23 eV. Instead of an endoergicity of 0.09 eV, the authors' method yields an exoergicity of 0.02 eV.

Fallon et al.[62] further introduce a new concept into the search for chromophores suitable for SF, excited state aromaticity.[65,66] It can be viewed as a subcategory of the more general concept of biradicaloid structure for SF described in the Introduction, applicable to systems derived from axial biradicals. In the general treatment,[25,33] a chromophore with $\Delta E(\mathrm{S}_1) = 2\ \Delta E(\mathrm{T}_1)$ is derived by covalent perturbation of a perfect biradical (a species with a doubly degenerate frontier orbital containing only two electrons), in which $\Delta E(\mathrm{S}_1) >> 2\ \Delta E(\mathrm{T}_1)$. Very strong covalent perturbation converts it into an ordinary molecule, in which $\Delta E(\mathrm{S}_1) < 2\ \Delta E(\mathrm{T}_1)$. For just the right strength of covalent perturbation, $\Delta E(\mathrm{S}_1) = 2\ \Delta E(\mathrm{T}_1)$, as desired for SF.

There are two limiting cases of perfect biradicals:[26] pair biradicals in which the exchange integral K_{AB} between the most localized choice of the frontier orbitals, A and B, is nearly or exactly zero (e.g., orthogonally twisted ethylene), and axial biradicals, in which K_{AB} equals K_{ab}, where a and b are the most delocalized real choice of frontier orbitals (e.g., O_2 or regular polygonal 4*N*-electron annulenes). There also are many intermediate cases, in which $0 < K_{\mathrm{AB}} < K_{\mathrm{ab}}$. Perfect biradicals of the 4*N*-electron annulene type, such as regularly octagonal cyclooctatetraene, are most strongly aromatic in the excited triplet state. As noted above, they yield $\Delta E(\mathrm{S}_1) >> 2\ \Delta E(\mathrm{T}_1)$ and are unsuitable, as are the too strongly covalently perturbed derivatives, which yield $\Delta E(\mathrm{S}_1) < 2\ \Delta E(\mathrm{T}_1)$. Suitable systems, for which $\Delta E(\mathrm{S}_1) = 2\ \Delta E(\mathrm{T}_1)$, need to be perturbed to an intermediate extent. The degree of triplet aromaticity as a measure of covalent perturbation can be approximately quantified using nucleus independent chemical shift (NICS) values. These are used by Fallon et al.,[62] who however do not specify clearly that a search for a structure with $\Delta E(S_1) = 2\ \Delta E(T_1)$ does not require a maximal nor a minimal triplet aromaticity as measured by the NICS value, but an intermediate one. A practical application of the procedure requires calculations of NICS values for a series of covalently perturbed perfect cyclic perimeters, and in most cases it would seem simpler to identify the optimal compound with $\Delta E(S_1) = 2\ \Delta E(T_1)$ by inspection of the calculated adiabatic excitation energies.

A limitation of the triplet aromaticity criterion is its restriction to biradicaloids derived from axial or nearly axial perfect biradicals. An example of such useful application is the consideration of diketopyrrolopyrroles,[62] formally derived from cyclooctatetraene via pentalene. In contrast, an attempted application[62] to biradicaloids of the type of **2**, formally derived from perfect pair biradicals, is not optimal in that it relies on arbitrarily selected resonance structures with 4*N* electrons in one of the rings, which can be always drawn for any conjugated aromatic or antiaromatic polycyclic system, even naphthalene.

Can SF in 2 be Enhanced? The observations made so far suggest very strongly that the fate of singlet excitons in **2a**, **2α**, and **2β** is primarily the formation of excimers and charge-transfer intermediates in processes that outcompete single-step SF from the singlet exciton directly to the biexciton (we cannot exclude the possibility that some fraction of the CT intermediates still undergo SF). This is disappointing, considering the promising molecular properties of **2**, but perhaps not surprising, given that Table 3 demonstrates that the slip-stacked crystal structures of **2α** and **2β** may well offer a reasonably large electronic matrix element for SF, but are also ideally set up for a large Davydov splitting that stabilizes the singlet exciton, thus hurting the SF energy balance and slowing down its rate tremendously. The existence of this stabilization is clearly seen in Figures 3 and S2. Moreover, the crystal structures **2α** and **2β** are perfectly preorganized for the formation of excimers by a slight motion, a mere reduction of the stacking distance combined with a slight slip. The local structure of the amorphous phase **2a** is likely to be similar even though a long-range order is missing.

Little if anything is known about the likely favored structure of the CT intermediate, but it appears quite possible that it is similar to the favored stacked excimer structure. After all, the CT intermediate can be viewed as a limiting case of an excimer in which locally excited configurations have higher energy than charge-separated configurations. Since the interaction element between the latter contains only the two-electron part of the Hamiltonian and is generally small (zero in the zero differential overlap approximation used in the program Simple), already a small asymmetry in the environment will cause one of the two charge-separated configurations to dominate, yielding a CT state. Similarly as in an excimer, stacking is favorable for electrostatic stabilization of charge-separated configurations.

It is thus tempting not to give up on **2** as a possible SF material yet, but to modify its molecular structure slightly by suitable substitution in an effort to enhance the rate of SF and slow down the formation of excimers and CT intermediates without damaging the favorable properties, such as light fastness and absorption characteristics. This might result in an improvement of molecular properties, in particular an increase in the T_1 - S_1 energy gap, and such effort could be guided by ordinary DFT calculations. We are especially intrigued by a possible improvement of molecular packing, with guidance provided by the very recently developed computer program Simple,[24,53] which calculates a set of desirable approximate target structures. It identifies all local maxima of SF rate in the physically realistic part of the six-dimensional space of all arrangements of a pair of rigid molecules. It uses many approximations, but as is seen in Figure 12, the calculated electronic matrix elements and magnitudes of Davydov splitting are in satisfactory agreement with the results of ab initio calculations. However, the guidance is not perfect, since the two-body approximation is used and many-body effects[67] are ignored, and since the rates of processes that compete with SF, such as excimer and CT intermediate formation, are not calculated. Nevertheless, Davydov splitting is evaluated and a qualitative estimate of the driving force for excimer and CT state formation is possible. Also the biexciton binding energy is calculated.

The twenty best pair geometries that maximize the square of the electronic matrix element for SF, $(T^{A})^2$, are listed in Table 4 and displayed in Figures 14, S15, and S16. They are slip-stacked and reminiscent of the actual crystal structures of **2α** and **2β**. They have very small biexciton binding energies, but with very few exceptions, they have a large Davydov splitting, on the order of 0.3 - 0.4 eV, dictated primarily by the interaction of the HOMO-LUMO transition densities on the two partners. This does not bode well for SF energy balance, and indeed, although these structures have large electronic matrix elements, they do not do well in the search for the local maxima of the SF rate constant.

The best 20 pair structures for maximum SF rate constants are listed in Table 3 and shown in Figures 13, S12, S13, and S14. They are quite different from the pair structures optimized for maximum $(T^{A})^2$ and from the observed crystal structures **2α** and **2β** (Figures 3 and S2). In most of them the two planar π systems are not stacked but lie at a considerable angle, and if they are stacked, they are also twisted. The Davydov splitting is much smaller and typical values are well below 0.1 eV. Moreover, the structures do not appear to be nearly as much predisposed for facile excimer formation. Although the latter observation is only qualitative, it is likely to be important. The biexciton binding energies remain small. It is clear that the avoidance of a large Davydov splitting and the associated less favorable SF energy balance are at least as essential for fast SF as a large electronic matrix element $(T^{A})^{2}$. Their importance has also been recognized by others.[68]

It is an interesting synthetic challenge to prepare one or more derivatives of **2** whose crystals would contain the motifs implied by the structures in Table 3 and Figures 13, S15, and S16, either because they spontaneously crystallize in an appropriate fashion or because they are dictated by the structure of a suitable covalent dimer of **2**.

Summary

The study of excited state dynamics in films of **2** is complicated by the presence of three distinct phases with similar but not identical properties, two crystalline and one amorphous, and by partial molecular alignment. We describe the combined use of X-ray diffraction and FT IR reflectance spectroscopy to unravel the composition of the films, and a simple procedure for dealing with the effects of the alignment. The photophysics is largely dominated by rapid evolution toward charge-transfer states and excimers at lower energies, which outcompetes SF. These species act as effective traps, but one or both yield triplets by intersystem crossing. The difference in the intermolecular geometries in the unit cells of the two polymorphs can be used to rationalize the experimental differences in kinetics and yields of the populations found in various excited states.

While the SF performance of the parent **2** is disappointing, it appears possible that a successful material could result from a minor modification of its structure, guided by the present

approximate calculations of optimal geometries that permit a complete search of the six-dimensional space of the geometrical arrangement of two rigid bodies. The reliability of the approximations used has been checked by comparison with the results of calculations by the ab initio Davydov-Frenkel exciton model at 48 local maxima of the SF rate.

Acknowledgement. This work was authored by Alliance for Sustainable Energy, LLC, the manager and operator of the National Renewable Energy Laboratory for the U.S. Department of Energy (DOE) under Contract No. DE-AC36-08GO28308. The US DOE, Basic Energy Sciences, Division of Chemical Sciences, Biosciences, and Geosciences, supported (i) the preparation and characterization of thin films at NREL, (ii) work at Brookhaven, through Grant DE-SC00112704, including use of the LEAF and Van de Graaff facilities of the BNL Accelerator Center for Energy Research, and (iii) work at the University of Colorado, Boulder, under award number DE-SC0007004. We used resources of the Advanced Light Source, which is a DOE Office of Science User Facility under contract no. DE-AC02-05CH11231. Work at the Institute of Organic Chemistry and Biochemistry in Prague was supported by the Institute (RVO: 61388963) and by GAČR grants 15-19143S and 19-22806S. This work is part of the (Shell-NWO) research programme (15CSER73) of the Foundation for Fundamental Research on Matter (FOM), which is part of the Netherlands Organisation for Scientific Research. RWAH acknowledges the FOM Focus group Groningen (NGOPV) for financial support.

Supporting Information. Sample preparation and characterization, crystallographic information, details of photophysics and pulse radiolysis, analysis of orientational effects, description of computation of pair geometries optimized for singlet fission by simple and ab initio methods, lists of optimized pair geometries, and TD-DFT results for **2** and its radical ions.

References

1. S. Singh, W. J. Jones, W. Siebrand, B. P. Stoicheff, and W. G. Schneider, J. Chem. Phys. **42**, 330 (1965).
2. M. Pope, N. E. Geacintov, and F. E. Vogel, Mol. Cryst. Liq. Cryst. **6**, 83 (1969).
3. M. C. Beard, J. C. Johnson, J. M. Luther, and A. J. Nozik, Philos. Trans. R. Soc. A **373**, 2014012 (2015).
4. M. B. Smith and J. Michl, Chem. Rev. **110**, 6891 (2010).
5. M. B. Smith and J. Michl, Annu. Rev. Phys. Chem. **64**, 361 (2013).
6. N. Monahan and X.-Y. Zhu, Annu. Rev. Phys. Chem. **66**, 601 (2015).
7. T. C. Berkelbach, Adv. Chem. Phys. **162**, 1 (2017).
8. E. A. Buchanan, Z. Havlas, and J. Michl, in *Advances in Quantum Chemistry: Ratner Volume, Volume 75*, edited by J. R. Sabin and E. J. Brändas, (Elsevier, Cambridge, MA, 2017), pp. 175-227. Erratum: In the last paragraph of section 2.5 (p. 205), delete $(h_A h_A|h_B h_B) + (h_A h_A|l_B l_B) + (l_A l_A|h_B h_B) + (l_A l_A|l_B l_B)$ in the expression for $|E(^1TT) - E(T+T)|$.
9. A. Rao and R. H. Friend, Nat. Rev. Mater. **2**, 17063 (2017).
10. D. Casanova, Chem. Rev. **118**, 7164 (2018).
11. K. C. Krishnapriya, A. J. Musser, and S. Patil, ACS Energy Lett. **4**, 192 (2019).
12. K. Miyata, F. S. Conrad-Burton, F. L. Geyer, and X.-Y. Zhu, Chem. Rev. **119**, 4261 (2019).
13. M. J. Y. Tayebjee, D. R. McCamey, and T. W. Schmidt, J. Phys. Chem. Lett. **6**, 2367 (2015).
14. W. Shockley and H. J. Queisser, J. Appl. Phys. **32**, 510 (1961).
15. M. C. Hanna and A. J. Nozik, J. Appl. Phys. **100**, 074510 (2006).
16. T. C. Berkelbach, M. S. Hybertsen and D. R. Reichman, J. Chem. Phys. **138**, 114103 (2013).
17. J. C. Johnson, A. J. Nozik and J. Michl, Acc. Chem. Res. **46**, 1290 (2013).

18. D. N. Congreve, J. Lee, N. J. Thompson, E. Hontz, S. R. Yost, P. D. Reusswig, M. E. Bahlke, S. Reineke, T. Van Voorhis, and M. A. Baldo, Science **340**, 334 (2013).
19. J. Lee, P. Jadhav, P. D. Reusswig, S. R. Yost, N. J. Thompson, D. N. Congreve, E. Hontz, T. Van Voorhis, and M. A. Baldo, Acc. Chem. Res. **46**, 1300 (2013).
20. N. J. Thompson, D. N. Congreve, D. Goldberg, V. M. Menon, and M. A. Baldo, Appl. Phys. Lett. **103**, 263302 (2013).
21. L. M. Pazos-Outon, J. M. Lee, M. H. Futscher, A. Kirch, M. Tabachnyk, R. H. Friend, and B. Ehrler, ACS Energy Lett. **2**, 476 (2017).
22. Z. Havlas and J. Michl, Isr. J. Chem. **56**, 96 (2016).
23. E. A. Buchanan and J. Michl, J. Am. Chem. Soc. **139**, 15572 (2017).
24. A. Zaykov, P. Felkel, E. A. Buchanan, M. Jovanovic, R. W. A. Havenith, R. K. Kathir, R. Broer, Z. Havlas, and J. Michl, *J. Am. Chem. Soc.*, in press.
25. I. Paci, J. C. Johnson, X. D. Chen, G. Rana, D. Popovic, D. E. David, A. J. Nozik, M. A. Ratner, and J. Michl, J. Am. Chem. Soc. **128**, 16546 (2006).
26. V. Bonačić-Koutecký, J. Koutecký, and J. Michl, Angew. Chem. Int. Ed. **26**, 170 (1987).
27. L. Salem and C. Rowland, Angew. Chem. Int. Ed. **11**, 92 (1972).
28. T. Minami and M. Nakano, J. Phys. Chem. Lett. **3**, 145 (2012).
29. T. Minami, S. Ito, and M. Nakano, J. Phys. Chem. Lett. **4**, 2133 (2013).
30. M. Nakano, Chem. Rec. **17**, 27 (2017).
31. S. Ito, T. Nagami, and M. Nakano, J. Phys. Chem. A **120**, 6236 (2016).
32. H. G. Viehe, Z. Janousek, R. Merényi, and L. Stella, Acc. Chem. Res. **18**, 148 (1985).
33. J. Wen, Z. Havlas, and J. Michl, J. Am. Chem. Soc. **137**, 165 (2015).
34. G. Engi, Angew. Chem. **27**, 144 (1914).

35. E. Valenta, Die Bunted Druckfarben, Wilhelm Knapp, Halle a. S., **1914**, p. 160.

36. L. Leonat, G. Sbarcea, and I. V. Branzoi, U.P.B. Sci. Bull., Series B **75**, 111 (2013).

37. J. S. de Melo, R. Rondao, H. D. Burrows, M. J. Melo, S. Navaratnam, R. Edge, and G. Voss, J. Phys. Chem. A **110**, 13653 (2006).

38. A. F. Morrison and J. M. Herbert, J. Phys. Chem. Lett. **8**, 1442 (2017).

39. W. N. Hansen, J. Opt. Soc. Am. **58**, 380 (1968).

40. K. Yamamoto and H. Ishida, Vibrational Specrtrosc. **8**, 1 (1994).

41. T. Hasegawa, S. Takeda, A. Kawaguchi, and J. Umemura, Langmuir **11**, 1236 (1995).

42. T. Hasegawa, J. Umemura, and T. Takenaka, J. Phys. Chem. **97**, 9009 (193).

43. F. Picard, T. Buffeteau, B. Desbat, M. Auger, and M. Pézolet, Biophys. J. **76**, 539 (1999).

44. A. Gericke, A. V. Michailov, and H. Hühnerfuss, Vibrational Spectrosc. **4**, 335 (1993).

45. K. Yamamoto and H. Ishida, Appl. Spectrosc. **7**, 775 (1994).

46. G. Kortüm, *Reflectance Spectroscopy: Principles, Methods, Applications* (Springer-Verlag, New York, 1969).

47. R. G. Greenler, J. Chem. Phys. **44**, 310 (1966). R. G. Greenler, J. Chem. Phys. **50**, 1963 (1969).

48. K. Yamamoto, A. Masui, and H. Ishida, Appl. Opts. **33**, 6285 (1994).

49. J. C. Johnson, A. J. Nozik, and J. Michl, J. Am. Chem. Soc. **132**, 16302 (2010).

50. J. Michl and E. W. Thulstrup, *Spectroscopy with Polarized Light. Solute Alignment by Photoselection, in Liquid Crystals, Polymers, and Membranes,* revised soft-cover edition (VCH Publishers, Deerfield Beach, Florida, 1995).

51. M. B. Mitchell, W. A. Guillory, J. Michl, and J. Radziszewski, Chem. Phys. Lett. **96**, 413 (1983).

52. S. Hirata and M. Head-Gordon, Chem. Phys. Lett. **314**, 291 (1999).

53. E. A. Buchanan, Z. Havlas, and J. Michl, *Bull. Chem. Soc. Jpn.*, published online September 9, 2019, http://dx.doi.org/10.1246/bcsj.20190229.

54. E. A. Buchanan and J. Michl, *Photoch. Photobio. Sci.* **2019**, *18*, 2112.

55. D. H. Arias, J. L. Ryerson, J. D. Cook, N. H. Damrauer, and J. C. Johnson, Chem. Sci. **7**, 1185 (2016).

56. R. E. Cook, B. T. Phelan, R. J. Kamire, M. B. Majewski, R. M. Young, and M. R. Wasielewski, J. Phys. Chem. A **121**, 1607 (2017).

57. P. I. Dron, J. Michl, and J. C. Johnson, J. Phys. Chem. A **121**, 8596 (2017).

58. C. B. Dover, J. K. Gallaher, L. Frazer, P. C. Tapping, and A. J. Petty, 2nd, M. J. Crossley, J. E. Anthony, T. W. Kee, and T. W. Schmidt, Nat. Chem. **10**, 305 (2018).

59. E. A. Margulies, J. L. Logsdon, C. E. Miller, L. Ma, E. Simonoff, R. M. Young, G. C. Schatz, and M. R. Wasielewski, J. Am. Chem. Soc. **139**, 663 (2017).

60. J. C. Johnson, A. Akdag, M. Zamadar, X. D. Chen, A. F. Schwerin, I. Paci, M. B. Smith, Z. Havlas, J. R. Miller, M. A. Ratner, A. J. Nozik, and J. Michl, J. Phys. Chem. B **117**, 4680 (2013).

61. E. A. Margulies, C. E. Miller, Y. Wu, L. Ma, G. C. Schatz, R. M. Young, and M. R. Wasielewski, Nat. Chem. **8**, 1120 (2016).

62. K. J. Fallon, P. Budden, E. Salvadori, A. M. Ganose, C. N. Savory, L. Eyre, S. Dowland, Q. Ai, S. Goodlett, C. Risko, D. O. Scanlon, C. W. M. Kay, A. Rao, R. H. Friend, A. J. Musser, and H. Bronstein, J. Am. Chem. Soc. **141**, 13867 (2019).

63. B. S. Basel, J. Zirzlmeier, C. Hetzer, B. T. Phelan, M. D. Krzyaniak, S. R. Reddy, P. B. Coto, N. E. Horwitz, R. M. Young, F. J. White, F. Hampel, T. Clark, M. Thoss, R R.

Tykwinski, M. R. Wasielewski, and D. M. Guldi, Nature Commun. **8**, 15171 (2017).

64. Z. E. X. Dance, M. J. Ahrens, A. M. Vega, A. B. Ricks, D. W. McCamant, M. A. Ratner, and M. R. Wasielewski, J. Am. Chem. Soc. **130**, 830 (2008).
65. N. C. Baird, J. Am. Chem. Soc. **94**, 4941 (1972).
66. H. Ottosson, Nat. Chem. **4**, 969 (2012).
67. E. A. Buchanan, J. Kaleta, J. Wen, S. H. Lapidus, I. Císařová, Z. Havlas, J. C. Johnson, and J. Michl, J. Phys. Chem. Lett. **10**, 1947 (2019).
68. A. K. Le, J. A. Benders, D. H. Arias, D. E. Cotton, J. C. Johnson, and S. T. Roberts, J. Am. Chem. Soc. **140**, 814 (2018).